High heat flux mapping using infrared images processed by inverse methods: an application to solar concentrating systems

Victor Pozzobon[1] ✉ **and Sylvain Salvador**[1]

[1]Université de Toulouse, centre RAPSODEE, UMR CNRS 5302, Mines Albi, Campus Jarlard, route de Teillet, 81013 CT Albi Cédex 09, France

With the spreading of solar concentrating devices and artificial suns, it has become critical to characterize the incident heat flux at the focal spot of such devices. In this paper a new method that allows the determination of incident heat flux at the focal spot concentrating devices has been developed. This approach is based on an inexpensive experimental device and basic inverse methods which are used to compute a map of the incident heat flux. The experimental setup is made of a common steel screen and an IR camera. Starting at ambient temperature, the screen is exposed to the incident heat flux. The evolution of the screen temperature field over time is recorded using the IR camera. The inverse model then uses temperature data to compute a map of the incident heat flux. Results at moderate heat flux were validated by comparison with Gardon radiometer readings: the agreement between the two methods is very good. This method yields a high resolution map without the need of an external scaling factor which is mandatory in the method using a CCD camera.

Concentrating solar system | Heat flux mapping | Inverse methods
Correspondence: ***victor.pozzobon@mines-albi.fr***

1. Introduction

Over the recent years interest in concentrated solar energy has grown. Indeed this source of power is able to achieve high heat flux and reach high temperatures. Thus it enables the study of high temperature (1, 2) or high heating rate (3) chemical processes, in order to better understand them. With time the use of solar concentrating devices has spread. Among them artificial suns are becoming more and more popular, as recently reviewed by Sarwar et al. (4). Indeed their power is available at will and their operating parameters do not vary during the day.

A key problem with operating these devices is the knowledge of the heat flux distribution on the target surface. This problem has been approached using various methods. In some cases a radiometer (5) or equivalent (6) is used to map the focal spot. Using this method is time consuming and offers a low spatial resolution map. Yet, it yields an absolute value of the incident heat flux and requires no external scaling factor. In other cases a CCD camera is used to record a grey value image of a water-cooled target (4, 7). Then using an external measurement, often a radiometer reading, a scaling factor is applied to the recorded image. This method allows for a high resolution but relies entirely on the external scaling factor and the use of a high-end water-cooled target. One last way of mapping the heat flux distribution is to run the device at minimal power, for example using the moon instead of the sun as an outdoor dish (8). Pictures can be taken and processed to yield high resolution incident heat flux map. Then, the actual map can be computed using the ratio of the two source powers. Sadly, this is not possible for certain devices such as Xenon arc lamps because their minimal power is very close to their nominal operating condition.

Heat flux distribution mapping is a widespread problem that can be found in numerous industrial problems. Among the various methods that have been developed for the determination of the incident heat flux, the inverse method is of particular interest. Inverse methods associate a problem, a mathematical model and experimental measurements to compute quantities of interest. These methods adopt a reverse point of view in comparison to the classical approaches. For example, a classical heat transfer problem is the determination of a temperature field from known boundary condition, heat source and material properties. This is called a direct problem. On the contrary, an inverse problem is the determination of boundary conditions, heat source and/or material properties from temperature measurements. A model linking the measurements to the desired value is built; it is called an inverse model. This approach has been applied with success to a wide variety of problems, such as the design of insulation protection (9), or the sizing of a heat exchanger (10).

In this paper a new, fast and simple method is proposed to map the incident heat flux distribution of an artificial sun. The required experimental setup is easy to handle and inexpensive. Using an IR camera, temperature variations of a common steel screen is recorded experimentally. The data are then processed using inverse method to accurately map the incident heat flux. The novelty of the method resides in the fact that it yields a high resolution map with none of the drawbacks of the existing methods (i.e. external scaling factor or high-end target). Finally, this method can be applied to the determination of external heat flux - radiative and/or convective - in 2D thermally thin problems such as heat exchanger design (10), fire safety problem where the incident heat flux on the surface has to be known, and plate cooling by evaporation in a burner.

2. Experimental setup

2 1. Materials

The studied image furnace is mounted with a 4 kW xenon arc lamp (Fig. 1). The lamp is set at the first focus of the elliptical mirror (semi major axis: 430 mm, semi minor axis: 205 mm). The elliptical mirror concentrates radiative power towards its second focus. To map the incident heat flux, a screen is set on the beams' trajectory to intercept them. As beams energy is absorbed by the screen, its temperature increases. The temperature variations are recorded by a 320x240 IR camera with a working range between 8 and 12 μm. Screen exposure is controled by a shutter placed on the light trajectory before the focal spot. The focal spot of this device is known to be 32 cm away from the lamp house casing.

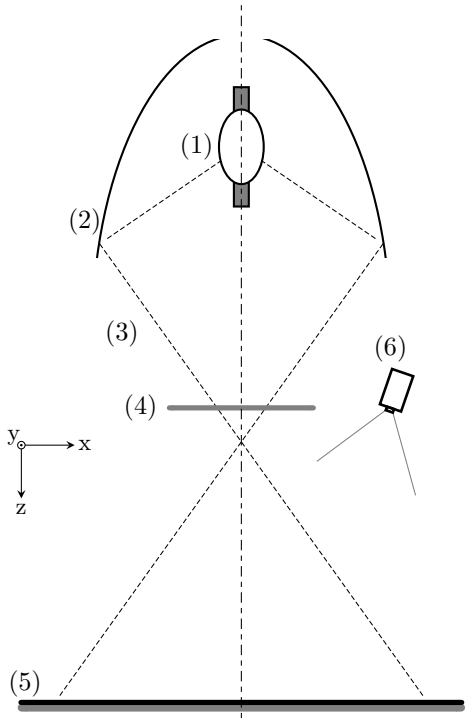

Fig. 1. Experimental apparatus schematics, defocused configuration. (1) - 4 kW xenon arc lamp, (2) - elliptical mirror, (3) - a ray, (4) - shutter, (5) - screen, (6) - camera, black line - paint

In order to have a flat emissivity of 0.79 in the camera working range, one side of the screen was painted with a black paint. Temperature was monitored on the painted side of the screen. Far from the focal spot, the painted side of the screen was illuminated (Fig. 1). At the focal spot, the bare steel side of the screen was illuminated reducing the absorbed energy by a factor of about 2 (Fig. 2).

2 2. Experimental procedure

The proposed inverse method requires transient screen temperature measurements. Indeed it uses the recording of the screen temperature elevation to yield a map of the incident heat flux. In this work, heat flux is mapped at the focal spot and also at several distances from the focal spot: 50, 75, 100, 125 and 150 cm. In order to assess repeatability, each measurement was repeated twice.

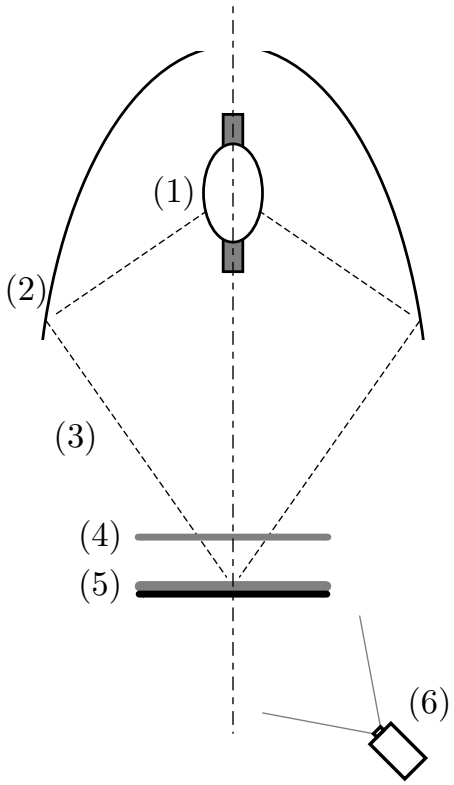

Fig. 2. Experimental apparatus schematics, focal spot configuration. (1) - 4 kW xenon arc lamp, (2) - elliptical mirror, (3) - a ray, (4) - shutter, (5) - screen, (6) - camera, black line - paint

For every run the following experimental procedure was observed:

- the screen and the camera are positioned,
- the shutter is closed,
- lamp is turned on,
- 10 minutes are waited for in order to get the lamp and lamp house thermally stable,
- the camera is started,
- the shutter is opened,
- the acquisition is turned off once critical temperatures are reached
- the shutter is closed

2 3. Experimental precautions

Because the camera was off the optical axis of the system, the pictures had to be corrected using a projective transformation before computing the incident heat flux.

In order to later simplify the problem, the screens were chosen to be thin and made out of a conductive material, so that temperature is almost constant in their thicknesses. Here, a 0.8 mm thick stainless steel square plate (304L steel) was used to produce the screens.

In cases where the screen is far from the focal spot (Fig. 1), its temperature does not increase much and its physical properties are assumed to remain constant. This assumption

implies that the screen temperature does not increase beyond reasonable bounds: 80 °C. This temperature was chosen to keep the screen thermal conductivity variation below 10 %. In this configuration, under moderate heat flux, the exposed side of the screen is painted black.

At the focal spot (Fig. 2), screen temperature increases sharply up to 300 °C within 3 s after which acquisition is stopped. Screen physical property variations was taken into account. Bare steel was exposed to incident heat flux, in order to take advantage of its reduced surface absorptivity and reduce the temperature increase speed so enough frames could be acquired before the screen reached 300 °C. Temperature was monitored on the other side that was painted black.

A Gardon radiometer was used to measure incident heat flux on the screen at different positions. These measurements allowed validation of the established inverse method results.

In our problem, it is critical to know several key spectral properties: the screen absorptivities with respect to the lamp spectrum and the screen emissivity with respect to the camera range. These properties were measured using a spectrometer and are available in Table 1.

Symbol	Name	Value	Dimension
α_p	Paint absorptivity	0.90	-
α_s	Steel absorptivity	0.48	-
ϵ_p	Paint emissivity	0.79	-
ϵ_s	Steel emissivity	0.48	-
ρ	Steel density	7900	kg/m^3
λ_0	Steel thermal conductivity	15	W/m/K
c_{p0}	Steel heat capacity	500	J/kg/K
e	Steel screen thickness	0.80	mm

Table 1. Physical properties of the screen

3. Direct model

In order to accurately describe the screen temperature evolution, the direct model has to account for interception of the incident heat flux, conduction inside of the screen, convective and radiative heat loss on the two faces. In this case, the temperature of the screen is governed by a classic 3D transient conduction model:

$$\rho c_p \frac{\partial T}{\partial t} = \lambda \Delta T \quad \textbf{(1)}$$

The set of boundary conditions are based on the the heat flux continuity. On the upper surface of the screen, incident heat flux, convective and radiative heat loss contribute to the heat flux:

$$-\lambda \nabla T.\vec{n} = -\alpha_p \phi + h(T - T_{sur}) + \epsilon_p \sigma (T^4 - T_{sur}^4) \quad \textbf{(2)}$$

With a surrounding temperature T_{sur} of 20 °C.

On the lower surface of the screen, convective and radiative heat losses govern the heat flux:

$$-\lambda \nabla T.\vec{n} = h(T - T_{sur}) + \epsilon_s \sigma (T^4 - T_{sur}^4) \quad \textbf{(3)}$$

On the side of the screen, thermal insulation can be assumed:

$$-\lambda \nabla T.\vec{n} = 0 \quad \textbf{(4)}$$

This classical conduction model can be simplified. Indeed, temperature inside the screen might be uniform in its thickness because the screen is very thin and made out of conductive material. Radiative Biot number based on the screen thickness can be calculated (Eq. 5). Under the most severe circumstances using ϕ_{max}, the Biot number remains below 0.1. Therefore, the temperature of the screen can be assumed to be homogeneous in its thickness.

$$Biot = \frac{\alpha_s \phi_{max} e}{\lambda \delta T} = 0.090 \quad \textbf{(5)}$$

The direct model can be simplified into a 2D transient model by inserting upper and lower surface boundary conditions (Ep. 2 and 3) as source terms in Eq. 1:

$$\rho c_p \frac{\partial T}{\partial t} = \lambda \Delta T + \frac{\alpha_p \phi}{e} - \frac{2h}{e}(T - T_{sur}) - \frac{(\epsilon_p + \epsilon_s)\sigma}{e}(T^4 - T_{sur}^4) \quad \textbf{(6)}$$

With the boundary condition on the side of the screen:

$$-\lambda \nabla T.\vec{n} = 0 \quad \textbf{(7)}$$

4. Inverse model

The inverse model (Eq. 8) was built based on the direct model. It enables the calculation of the incident heat flux ϕ and the convective heat transfer coefficient h for each pixel. Thus it yields a map of the incident heat flux. The idea behind the inverse model is to calculate the gap (called *observable* $y_{i,j}^k$) between the measured increase in temperature and the contribution of heat diffusion and radiation losses. This gap is directly associated to the contribution of the incident heat flux and the convective loss. Then using ordinary least square method (11), heat flux and convective heat transfer coefficient are computed to minimize this gap. Thus, the best fitting heat flux $\hat{\phi_{i,j}}$ and convective heat transfer coefficient $\hat{h_{i,j}}$ are determined for each pixel. In the present work, for the sake of simplicity, it is assumed that both ϕ and h are constant in time for a given pixel.

The observable $y_{i,j}^k$ can be written for each pixel at each time step as follows:

$$y_{i,j}^k = T_{i,j}^{k+1} - T_{i,j}^k - dt \frac{\lambda}{\rho c_p} \Delta T_{i,j}^k - dt \frac{(\epsilon_p + \epsilon_s)\sigma}{\rho c_p e}((T_{i,j}^k + 273)^4 - (T_{sur} + 273)^4) \quad \textbf{(8)}$$

Where, the Laplacian operator is computed using central finite differences scheme:

$$\Delta T_{i,j}^k = T_{i+1,j}^k + T_{i-1,j}^k - 4T_{i,j}^k + T_{i,j+1}^k + T_{i,j-1}^k \quad \textbf{(9)}$$

For a given pixel, the observable is written as follows:

$$\boldsymbol{y}_{i,j} = \begin{pmatrix} y_{i,j}^{1} \\ \vdots \\ y_{i,j}^{k} \\ \vdots \\ y_{i,j}^{n-1} \end{pmatrix} \quad \textbf{(10)}$$

A sensitivity matrix $\boldsymbol{X}_{i,j}$ has to be built and inversed for every pixel. This matrix is the mathematical object which contains the contribution of the incident heat flux and the convective loss.

$$\boldsymbol{X}_{i,j} = \begin{pmatrix} \frac{dt\alpha}{\rho c_p e} & -\frac{2dt}{\rho c_p e}(T_{i,j}^{1} - T_{sur}) \\ \vdots & \vdots \\ \frac{dt\alpha}{\rho c_p e} & -\frac{2dt}{\rho c_p e}(T_{i,j}^{k} - T_{sur}) \\ \vdots & \vdots \\ \frac{dt\alpha}{\rho c_p e} & -\frac{2dt}{\rho c_p e}(T_{i,j}^{n-1} - T_{sur}) \end{pmatrix} \quad \textbf{(11)}$$

Then, the system can be inverted using simple matrix operations yielding the incident heat flux and the convective coefficient maps:

$$\begin{pmatrix} \hat{\phi_{i,j}} \\ \hat{h_{i,j}} \end{pmatrix} = (X_{i,j}^{T} X_{i,j})^{-1} X_{i,j}^{T} y_{i,j} \quad \textbf{(12)}$$

The inverse method approach has two major advantages that are underlined here. First, on the contrary to CCD camera heat flux measurements, it does not require an external scaling factor. This factor being most of the time provided by a radiometer (1, 4). Second, distance temperature measurement encounters a reflexion problem. Indeed when the target is exposed to an incident heat flux, a fraction of this heat flux is reflected toward the captor. Thus the measured temperature is the sum of the actual temperature and the reflected heat flux contribution. Precaution has to be taken in order to accurately monitor temperature (12, 13). In the present work, by building the observable using temperatures differences, the additive contribution of the reflected heat flux to the monitored temperature is nullified.

The thermal properties of the target material were set as follows. As stated before, the screen temperature remains relatively low. It allows to reasonably assume that screen physical properties are constant. Values of the screen thermal conductivity and heat capacity can be found in Table 1. On the contrary, at the focal spot, screen temperature increases sharply up to 300 °C. Thus physical properties could not be assumed to be constant and the following correlations (14) were used to describe screen thermal conductivity and heat capacity evolution with temperature:

$$\lambda(T(K)) = 7.9318 + 0.023051T - 6.4166 \times 10^{-6} T^2 \ \ W/m/K \quad \textbf{(13)}$$

$$Cp(T(K)) = 426.7 + 1.700 \times 10^{-1} T + 5.200 \times 10^{-5} T^2 \ \ J/kg/K \quad \textbf{(14)}$$

5. Results

It is common in the inverse method field to check the inverse algorithm capabilities with simulated values (15). The direct model was computed with a prescribed heat flux. Then noise was added to the produced temperature data and finally the inverse algorithm was run. The agreement between actual values and estimated values of the incident heat flux was very good. From there, heat flux distribution were estimated from IR measurements for various distances ranging from z=0 to z=150 cm from the focal spot.

Figure 3 reports the determined heat flux contour map 100 cm away from the focal spot. One can see that the incident heat flux has a ring shape with a higher heat flux on the right hand side of the map. These discrepancies are attributed to error in the geometrical adjustment of the lamp and the mirror.

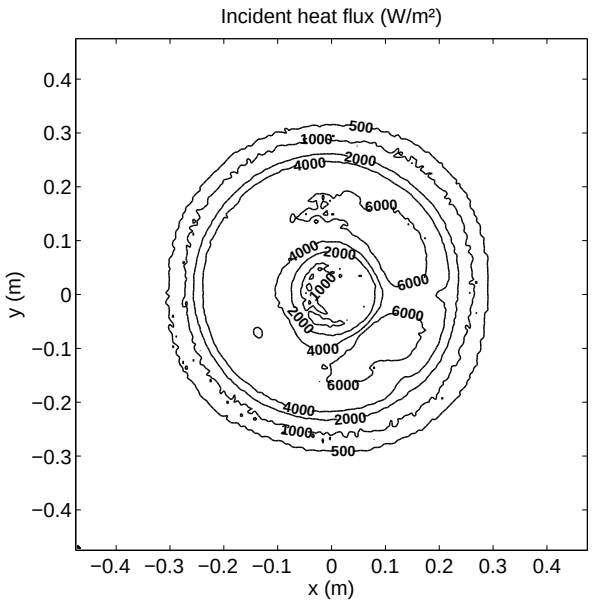

Fig. 3. Heat flux mapping 1 m away from the focal spot

A Gardon radiometer was used to measure heat flux along the horizontal and vertical axes as a test to validate the inverse method estimation. Figures 4 and 5 compare the inverse method results with Gradon radiometer measurements. Both methods yield very close results. Moreover the inverse method provides at a time higher spatial resolution heat flux map than the Gardon radiometer measurements.

Figure 6 reports the determined heat flux distribution at the focal spot. The spatial distribution has a maximum of 1335 kW/m^2 and a diameter of about 3 cm. Figure 7 reports the heat flux distribution along x and y axes. These very similar distributions exhibit a Gaussian shape, which is congruent with literature (4, 5, 7).

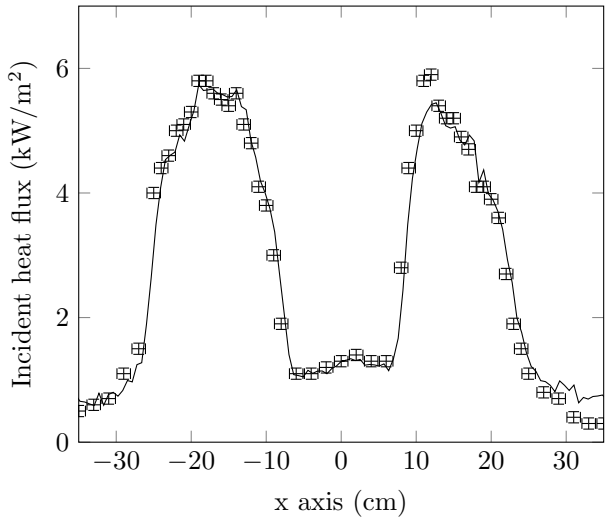

Fig. 4. Heat flux 1 m away from the focal spot on the **x axis**. Continuous line - from inverse method, crosses with error bars - from Gardon radiometer

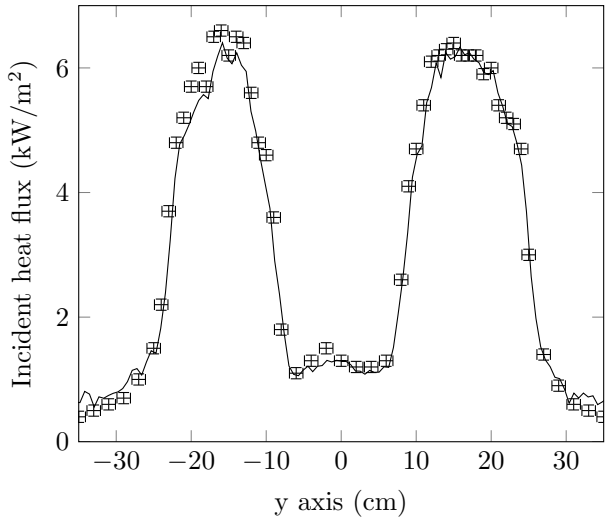

Fig. 5. Heat flux 1 m away from the focal spot on the **y axis**. Continuous line - from inverse method, crosses with error bars - from Gardon radiometer

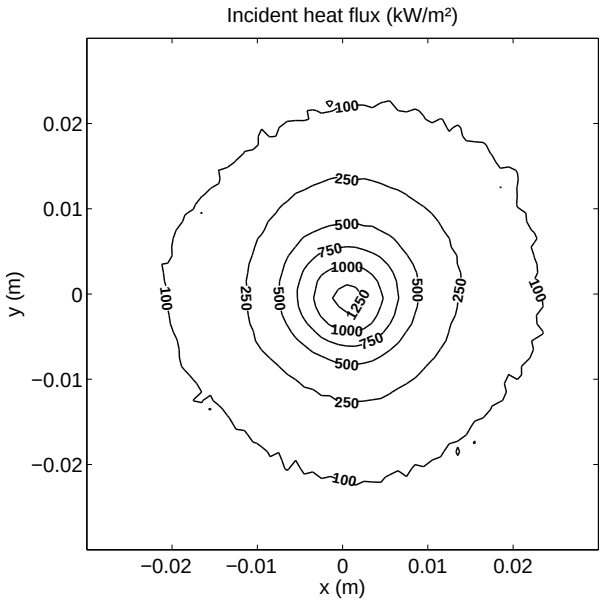

Fig. 6. Heat flux mapping at the focal spot

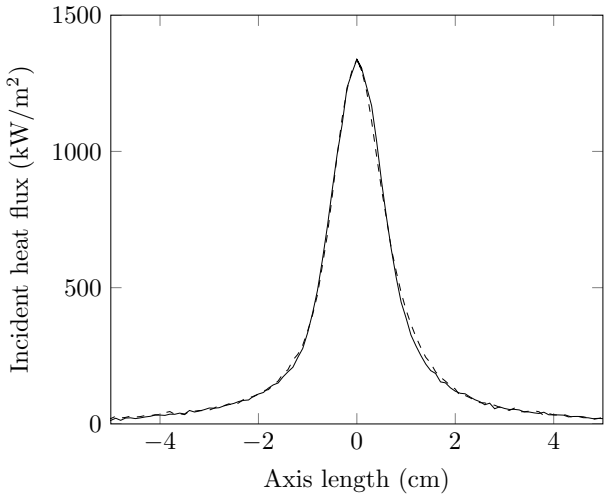

Fig. 7. Heat flux distribution at the focal spot. Continuous line - x axis, dashed line - y axis

The beam total power is obtained by integrating the heat flux over the screen surface. Figure 8 reports the beam power variation as a function of the distance of the target to the focal spot. The incident power away from the focal spot exhibits small variations of $\pm$ 5 % around an average value of 966 W. The accuracy of the presented measurements are thought to be very good.

Repeatability was assessed using the two measurements made for each distance. Figure 9 reports the deviation between two runs: it is lower than 5 % in the regions where signal-to-noise ratio is good i.e. area with high incident heat flux. The discrepancy increases in low heat flux areas, which can be explained by the fact that the temperature rise is small in these regions: in this case, the sensibility coefficient associated to convective heat loss tends towards zero (Eq. 15) which lowers inverse method predictions quality and therefore repeatability.

$$\lim_{T_{i,j}^k \to T_{sur}} -\frac{2dt}{\rho c_p(T_{i,j}^k)e}(T_{i,j}^k - T_{sur}) = 0 \qquad \textbf{(15)}$$

6. Conclusion and perspectives

In this paper, inexpensive and easy to handle experiments were used to rapidly map the heat flux map of a solar concentrating device. A screen made of a thin widespread painted steel plate was exposed to the incident heat flux. An IR camera was used to record the screen temperature field. IR images sequences were processed using basic inverse method approach and yield incident heat flux distribution. As the screen spectral properties were known, no external scaling factor was needed.

Results obtained far from the focal spot were validated by comparison with Gardon radiometer readings: the agreement

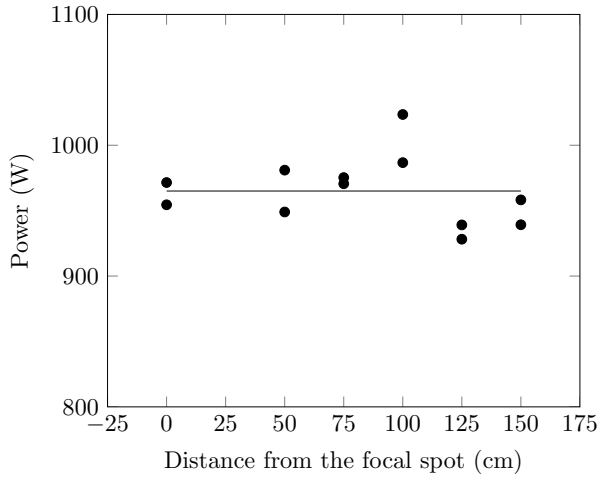

Fig. 8. Incident power for all runs. Dot - individual value, continuous line - average value

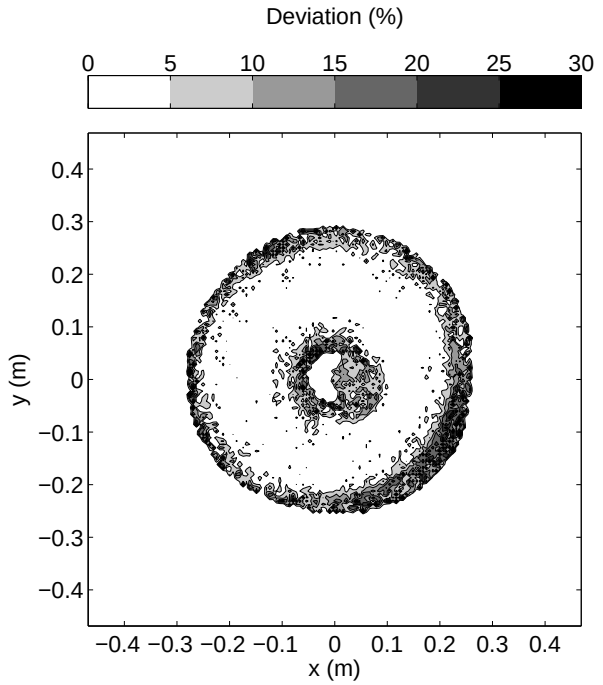

Fig. 9. Typical deviation between two runs 1 m away from the focal spot

between the two methods is very good. The computed beam total power has also been shown to be the same for several distances of the screen to the focal spot. Finding that total power is conservative is a token of the good quality of the proposed method.

In this work, the inverse method was used on a basic level. Using more advanced techniques, the incident heat flux can be further characterized. Among the critical possible improvements, time variability of the heat flux is of note. Indeed using more sophisticated approaches (9, 16, 17), it would be possible to compute a time dependent incident heat flux and convective heat transfer coefficient for every pixel.

Another point is the IR camera resolution. In our case the camera resolution was quite low: 320x240. A greater resolution would lead to a more precise heat flux map and to a better calculation of the Laplacian operator, reducing the impact of noise on the computed heat flux.

Acknowledgement

This work was funded by the French "Investments for the future" program managed by the National Agency for Research under contract ANR-10-LABX-22-01. We would like to thank Olivier Fudym for his help in operating the IR camera and Mickael Ribeiro for his technical support.

Latin symbols		
c_p	screen specific heat capacity	J/kg/K
dt	time between two frames	s
e	screen thickness	m
h	convective heat transfer coefficient	W/m^2/K
$\vec{n}$	normal vector	-
T	temperature	°C
t	time	s
Greek symbols		
α	absorptivity	-
δT	temperature difference	°C
Δ	Laplacian operator	1/m^2
ϵ	emissivity	-
λ	screen thermal conductivity	W/m/K
ρ	screen density	kg/m^3
σ	Stefan-Boltzmann constant	W/m^2/K^4
ϕ	incident heat flux	W/m^2
Subscripts		
i	frame pixel index in x direction	
j	frame pixel index in y direction	
ols	estimated using ordinary least square	
p	paint	
s	bare steel	
sur	surrounding	
Superscripts		
k	frame time index	
n	total number of frame	
T	matrix transposition operator	
$\hat{}$	ordinary least square estimator	

Table 2. Nomenclature

References

1. C. Guesdon, I. Alxneit, H. R. Tschudi, D. Wuillemin, and M. Sturzenegger. 1 kW imaging furnace with in situ measurement of surface temperature. *Review of Scientific Instruments*, 77(3):035102, March 2006. ISSN 0034-6748. . WOS:000236739100040.
2. A. Imhof. Decomposition of limestone in a solar reactor. *Renewable Energy*, 10(2–3):239–246, 1997. ISSN 0960-1481. .
3. Olivier Authier, Monique Ferrer, Guillain Mauviel, Az-Eddine Khalfi, and Jacques Lede. Wood Fast Pyrolysis: Comparison of Lagrangian and Eulerian Modeling Approaches with Experimental Measurements. *Industrial & Engineering Chemistry Research*, 48(10):4796–4809, May 2009. ISSN 0888-5885. . WOS:000266081300016.
4. Jawad Sarwar, Grigoris Georgakis, Robert LaChance, and Nesrin Ozalp. Description and characterization of an adjustable flux solar simulator for solar thermal, thermochemical and photovoltaic applications. *Solar Energy*, 100:179–194, February 2014. ISSN 0038-092X. . WOS:000331007700018.
5. J. Llorente, J. Ballestrin, and A. J. Vazquez. A new solar concentrating system: Description, characterization and applications. *Solar Energy*, 85(5):1000–1006, May 2011. ISSN 0038-092X. . WOS:000290644000029.
6. Daniel S. Codd, Andrew Carlson, Jennifer Rees, and Alexander H. Slocum. A low cost high flux solar simulator. *Solar Energy*, 84(12):2202–2212, December 2010. ISSN 0038-092X. .
7. Joerg Petrasch, Patrick Coray, Anton Meier, Max Brack, Peter Haeberling, Daniel Wuillemin, and Aldo Steinfeld. A novel 50 kW 11,000 suns high-flux solar simulator based on an array of xenon arc lamps. *Journal of Solar Energy Engineering-Transactions of the Asme*, 129(4): 405–411, November 2007. ISSN 0199-6231. . WOS:000250637900008.

8. N.D. Kaushika and S. Kaneff. Flux distribution and intercept factors in the focal region of paraboloidal dish concentrators. In *Proc. ISES Solar World Congress*, volume 2, pages 1607–1611, Hamburg, 1987.
9. M. Mohammadiun, A. B. Rahimi, and I. Khazaee. Estimation of the time-dependent heat flux using the temperature distribution at a point by conjugate gradient method. *International Journal of Thermal Sciences*, 50(12):2443–2450, December 2011. ISSN 1290-0729. .
10. Zhaohong Fang, Donglai Xie, Nairen Diao, John R. Grace, and C. Jim Lim. A new method for solving the inverse conduction problem in steady heat flux measurement. *International Journal of Heat and Mass Transfer*, 40(16):3947–3953, October 1997. ISSN 0017-9310. .
11. Helcio R. B. Orlande, Olivier Fudym, Denis Maillet, and Renato M. Cotta, editors. *Thermal Measurements and Inverse Techniques*. CRC Press, Boca Raton, FL, May 2011. ISBN 9781439845554.
12. D. Hernandez, G. Olalde, J. M. Gineste, and C. Gueymard. Analysis and experimental results of solar-blind temperature measurements in solar furnaces. *Journal of Solar Energy Engineering-Transactions of the Asme*, 126(1):645–653, February 2004. ISSN 0199-6231. . WOS:000189287100013.
13. J. Ballestrín, M. Rodríguez-Alonso, J. Rodríguez, I. Cañadas, F. J. Barbero, L. W. Langley, and A. Barnes. Calibration of high-heat-flux sensors in a solar furnace. *Metrologia*, 43(6): 495, December 2006. ISSN 0026-1394. .
14. R. S. Graves, T. G. Kollie, D. L. McElroy, and K. E. Gilchrist. The thermal conductivity of AISI 304l stainless steel. *International Journal of Thermophysics*, 12(2):409–415, March 1991. ISSN 0195-928X, 1572-9567. .
15. Chunli Fan, Fengrui Sun, and Li Yang. Simple Numerical Method for Multidimensional Inverse Identification of Heat Flux Distribution. *Journal of Thermophysics and Heat Transfer*, 23(3):622–629, September 2009. ISSN 0887-8722. . WOS:000268300300023.
16. You-An Shi, Lei Zeng, Wei-Qi Qian, and Ye-Wei Gui. A data processing method in the experiment of heat flux testing using inverse methods. *Aerospace Science and Technology*, 29(1):74–80, August 2013. ISSN 1270-9638. .
17. H. M. Park and W. S. Jung. On the solution of multidimensional inverse heat conduction problems using an efficient sequential method. *Journal of Heat Transfer-Transactions of the Asme*, 123(6):1021–1029, December 2001. ISSN 0022-1481. . WOS:000172645400001.